PHYSICAL REVIEW C **88**, 024308 (2013)

Further explorations of Skyrme-Hartree-Fock-Bogoliubov mass formulas. XIII. The 2012 atomic mass evaluation and the symmetry coefficient

S. Goriely,[1] N. Chamel,[1] and J. M. Pearson[2]

[1]*Institut d'Astronomie et d'Astrophysique, CP-226, Université Libre de Bruxelles, 1050 Brussels, Belgium*

[2]*Département de Physique, Université de Montréal, Montréal, Québec, H3C 3J7 Canada*

(Received 28 March 2013; revised manuscript received 21 June 2013; published 7 August 2013)

Our family of three Hartree-Fock-Bogoliubov (HFB) mass models, labeled BSk19, BSk20, and BSk21, is here extended by (a) refitting to the 2012 Atomic Mass Evaluation (AME), and (b) varying the symmetry coefficient J. Five new models, labeled BSk22 to BSk26, along with their mass tables, HFB-22 to HFB-26, respectively, are presented. These models are characterized by unconventional Skyrme forces containing t_4 and t_5 terms, i.e., density-dependent generalizations of the usual t_1 and t_2 terms, respectively. Highly realistic contact pairing forces are used. The Skyrme forces are constrained to fit realistic equations of state of neutron matter stiff enough to support the massive neutron stars PSR J1614$-$2230 and PSR J0348 + 0432. Unphysical spin and spin-isospin instabilities of homogeneous nuclear matter, including the transition to a polarized state in neutron-star matter, are eliminated with the new forces. The best fits to the new database of 2353 nuclei are found for models BSk24 ($J = 30$ MeV) and BSk25 ($J = 29$ MeV), for which the root-mean square (rms) deviations are 0.55 and 0.54 MeV, respectively. Despite the larger database this is even better than the rms deviation of 0.58 MeV that we found with our fits to the 2003 AME. With $J = 32$ MeV the rms deviation rises to 0.63 MeV. The neutron-skin thicknesses derived from antiproton scattering are shown to be consistent with the conclusions that we have drawn from masses.

DOI: 10.1103/PhysRevC.88.024308 PACS number(s): 21.10.Dr, 21.30.$-$x, 21.60.Jz, 26.60.Kp

I. INTRODUCTION

In Ref. [1] we presented a family of three Skyrme-type functionals, BSk19, BSk20, and BSk21, along with their corresponding mass tables, HFB-19, HFB-20, and HFB-21, respectively, that we had constructed with a view to providing a unified approach not only to the structure of all the different regions of neutron stars (outer crust, inner crust, and core) but also to other phenomena associated with the birth and death of neutron stars, such as supernova-core collapse, the r-process of nucleosynthesis in the neutrino-driven wind, and nucleosynthesis via the decompression of neutron-star matter. These three functionals are all based on effective forces with the 16-parameter generalized Skyrme form shown in Eq. (1), which is characterized by unconventional terms that have a simultaneous density and momentum dependence.

The parameters of this form of force were determined primarily by fitting measured nuclear masses, which were calculated with the Hartree-Fock-Bogoliubov (HFB) method. For this it was necessary to supplement the Skyrme forces with a microscopic pairing force, phenomenological Wigner terms and correction terms for the spurious collective energy. However, in fitting the mass data we simultaneously constrained the Skyrme force to fit the zero-temperature equation of state (EOS) of infinite homogeneous neutron matter (NeuM), as determined by many-body calculations with realistic two- and three-nucleon forces. Actually, several realistic calculations of the EOS of NeuM have been made, and while they all agree fairly closely at nuclear and subnuclear densities, at the much higher densities that can be encountered towards the center of neutron stars they differ greatly in their stiffness, and there are very few data, either observational or experimental, to discriminate between the different possibilities (see Fig. 1). It is in this way that we arrived at our three different functionals, as follows.

BSk19 is the softest of our functionals in high-density NeuM, being constrained to the EOS of Friedman and Pandharipande [2] (FP), which is based on a variational calculation using the realistic Urbana v_{14} nucleon-nucleon force with the three-body force TNI. BSk20 has intermediate stiffness, as it is constrained to the EOS of Akmal *et al.* [3] labeled "A18 + $\delta\, v$ + UIX*", which we refer to as APR. This EOS, like FP, is based on a variational calculation but uses the more up-to-date realistic Argonne A18 two-body force and the semiphenomenological UIX* three-body force; there is also a so-called relativistic boost correction $\delta\, v$. Finally, our stiffest functional, BSk21, is constrained to the EOS labeled "V18" in Ref. [4], which we refer to as LS2. It is based on the same A18 two-body force as is APR, but uses a much more realistic three-body force and is calculated with the Brueckner-Hartree-Fock (BHF) method. Ref. [5] has also drawn attention to the question of high-density stiffness of the EOS.

We also imposed the following additional constraints: (a) an optimal fit to the charge-radii data [6], (b) a value of $0.8M$ for the isoscalar effective mass M_s^* in charge-symmetric infinite homogeneous nuclear matter (INM) at the appropriate equilibrium density n_0, this being the value indicated by calculations on INM with realistic forces (see the discussion in Ref. [7]), (c) an incompressibility K_v of charge-symmetric INM falling in the experimental range 240 ± 10 MeV [8], (d) the stability of NeuM and of β-equilibrated neutron-star matter (i.e., the homogeneous nucleon-lepton mixture of which neutron-star cores are comprised) against an unphysical polarization at any density relevant to neutron-star cores [9,10], (e) an EOS of charge-symmetric INM that is consistent with measurements in heavy-ion collisions of nuclear-matter flow

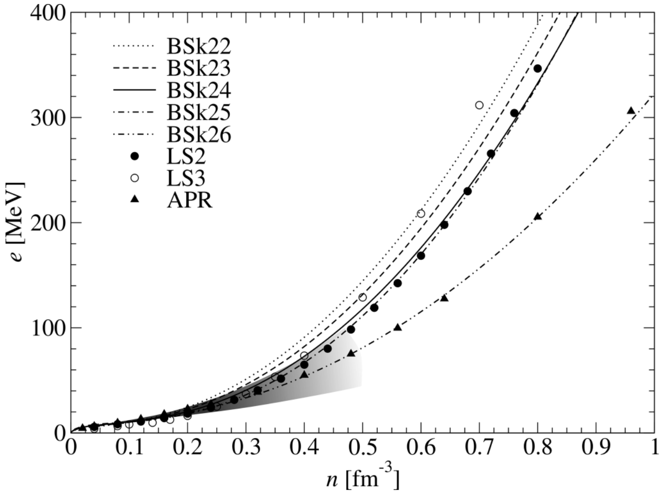

FIG. 1. Zero-temperature EOSs for neutron matter with models BSk22–26. APR is the realistic EOS "A18 + $\delta\, v$ + UIX*" in Ref. [3]. LS2 and LS3 correspond to the realistic EOSs referred to as V18 and BOB in Ref. [4], respectively. The shaded area represents the constraints obtained in Ref. [32].

over the density range 1.5–4.5n_0 [11,12], (f) a qualitatively acceptable distribution of potential energy among the four different spin-isospin channels in INM.

The form of our functionals is sufficiently flexible to allow all these constraints to be satisfied and at the same time for the 2149 measured masses of nuclei with N and $Z \geqslant 8$ given in the 2003 Atomic Mass Evaluation (AME) [13] to be fitted with an root mean square (rms) deviation as low as 0.58 MeV with all three models, i.e., with all three options for the high-density variation of the energy per nucleon of NeuM. However, there have been two significant developments since the time that these functionals and their associated mass models were constructed.

The neutron star PSR J1614−2230, and more recently PSR J0348 + 0432, have been shown to have a mass as high as 1.97 ± 0.04 $\mathcal{M}_\odot$ for the former [14] and 2.01 ± 0.04 $\mathcal{M}_\odot$ for the latter [15]. Now in Ref. [16] we solved the Tolman-Oppenheimer-Volkoff (TOV) equations [17,18] to determine the maximum possible neutron-star mass for each of our models. As will be seen in the first three lines of Table I, the EOS obtained with BSk19 is definitely too soft, and is discarded, along with the EOS of FP.

At the end of 2012 a new AME [19] was published, with 2353 measured masses of nuclei having N and $Z \geqslant 8$. (This set contains both nuclei whose masses are measured for the first time, and also nuclei whose previously quoted masses have been revised; 15 nuclei for which measured masses appeared in the 2003 AME no longer have this status.) Now when we calculate the rms deviation for HFB-20 and HFB-21 with respect to this new data set, we find that it rises by 17 keV for the former and falls by 5 keV for the latter, which means that the new data distinguish between the two EOSs, favoring LS2 over APR, at least for nuclear densities. (The fact that the rms deviation in the case of HFB-21 is actually lower for the larger data base of the 2012 AME than for the 2003 AME, to which it was fitted, is an indicator of the reliability with which this model can be extrapolated into unknown regions of the nuclear chart.)

TABLE I. Maximum neutron-star mass for different models.

Force	$\mathcal{M}_{\max}/\mathcal{M}_\odot$
BSk19	1.86
BSk20	2.15
BSk21	2.28
BSk22	2.26
BSk23	2.27
BSk24	2.28
BSk25	2.22
BSk26	2.15

Clearly, it is desirable to refit the HFB-21 model to the 2012 AME. This we do in the present paper, but we also take the opportunity of addressing an issue that was neglected in Ref. [1], namely, that of the symmetry coefficient J. Previously, we took $J = 30$ MeV, this being the most plausible value that emerged from some preliminary trial calculations, but here we examine the question much more thoroughly, considering also $J = 29$, 31 and 32 MeV. For each of these four values of J we shall take LS2 for the constraining EOS, although in one case, $J = 30$ MeV, we shall also constrain to APR, in order to check that our conclusion concerning the superiority of LS2 remains valid after refitting to the larger data set.

In Sec. II we review the essential features of our models, while the results of our new fits are described in Sec. III, with the impact of the new AME and the sensitivity to the symmetry coefficient J both being discussed; this section also examines the neutron-skin thicknesses predicted by our new models. Section IV contains our conclusions.

II. PRINCIPAL FEATURES OF OUR HFB CALCULATIONS

The new models introduced here are identical in form to the ones of Ref. [1]. We recall here the essential features.

(i) The form of our generalized Skyrme force is

$$\begin{aligned} v_{ij} = {}& t_0(1+x_0P_\sigma)\delta(\boldsymbol{r}_{ij}) + \frac{1}{2}t_1(1+x_1P_\sigma)\frac{1}{\hbar^2}\left[p_{ij}^2\,\delta(\boldsymbol{r}_{ij}) + \delta(\boldsymbol{r}_{ij})\,p_{ij}^2\right] + t_2(1+x_2P_\sigma)\frac{1}{\hbar^2}\,\boldsymbol{p}_{ij}.\delta(\boldsymbol{r}_{ij})\,\boldsymbol{p}_{ij} \\ & + \frac{1}{6}t_3(1+x_3P_\sigma)\,n(\boldsymbol{r})^\alpha\,\delta(\boldsymbol{r}_{ij}) + \frac{1}{2}\,t_4(1+x_4P_\sigma)\frac{1}{\hbar^2}\left[p_{ij}^2\,n(\boldsymbol{r})^\beta\,\delta(\boldsymbol{r}_{ij}) + \delta(\boldsymbol{r}_{ij})\,n(\boldsymbol{r})^\beta\,p_{ij}^2\right] \\ & + t_5(1+x_5P_\sigma)\frac{1}{\hbar^2}\,\boldsymbol{p}_{ij}.n(\boldsymbol{r})^\gamma\,\delta(\boldsymbol{r}_{ij})\,\boldsymbol{p}_{ij} + \frac{\mathrm{i}}{\hbar^2}W_0(\boldsymbol{\sigma_i}+\boldsymbol{\sigma_j})\cdot\boldsymbol{p}_{ij}\times\delta(\boldsymbol{r}_{ij})\,\boldsymbol{p}_{ij}, \end{aligned} \tag{1}$$

where $\boldsymbol{r}_{ij} = \boldsymbol{r}_i - \boldsymbol{r}_j$, $\boldsymbol{r} = (\boldsymbol{r}_i + \boldsymbol{r}_j)/2$, $\boldsymbol{p}_{ij} = -i\hbar(\nabla_i - \nabla_j)/2$ (this is the relative momentum), P_σ is the two-body spin-exchange operator, and $n(\boldsymbol{r}) = n_n(\boldsymbol{r}) + n_p(\boldsymbol{r})$ is the total local density, $n_n(\boldsymbol{r})$ and $n_p(\boldsymbol{r})$ being the neutron and proton densities, respectively. The t_4 and t_5 terms are unconventional, being density-dependent generalizations of the t_1 and t_2 terms, respectively. The full formalism for this generalized Skyrme force is presented in the Appendix of Ref. [9], but note that we now drop all the terms quadratic in the spin current tensor and their time-odd counterpart from the Hamiltonian density, as discussed in Ref. [1]. We found that those terms are generally at the origin of spurious instabilities.

(ii) Our pairing force has a δ-function form,

$$v_q^{\mathrm{pair}}(\boldsymbol{r}_i, \boldsymbol{r}_j) = f^{\pi\, q} v[n_n(\boldsymbol{r}), n_p(\boldsymbol{r})]\delta(\boldsymbol{r}_{ij}), \tag{2}$$

where $v[n_n, n_p]$ is a functional of both the neutron and proton densities, calculated analytically at each point in the nucleus in question in such a way as to reproduce the ${}^1S_0$ pairing gaps of INM of the appropriate density and charge asymmetry, as determined by many-body calculations with realistic two- and three-nucleon forces [20,21]. (Note that an analytic representation of the function $v[n_n(\boldsymbol{r}), n_p(\boldsymbol{r})]$ is now available [22].) The INM constraint determines the strength of the pairing force almost completely, but we introduce some fine-tuning of the strengths in the form of the four global renormalization parameters $f^{\pi\, q}$, which allow the overall strength to be slightly different for neutrons than for protons, and which also permit each of these strengths to depend on whether there is an even or odd number of nucleons of the charge type in question. In this way we take into account Coulomb effects as well as the slight violation of time-reversibility implicit in our treatment of odd nuclei (see below). With the purely bulk picture of pairing that we are adopting the renormalization parameter for an even number of neutrons must be taken to be equal to 1. A cutoff parameter ε_Λ to the single-particle (s.p.) spectrum is introduced, as described in Ref. [20].

(iii) We subtract from the HFB energy an estimate for the spurious collective energy. As described in Ref. [20], the form we adopt here (and in Ref. [1]) is

$$E_{\mathrm{coll}}{=}E_{\mathrm{rot}}^{\mathrm{crank}}\left\{b\tanh(c|\beta_2|) + d|\beta_2|\exp\left\{-l\left(|\beta_2| - \beta_2^0\right)^2\right\}\right\}, \tag{3}$$

in which $E_{\mathrm{rot}}^{\mathrm{crank}}$ denotes the cranking-model value of the rotational correction and β_2 the quadrupole deformation. The parameters b and c have been determined by fitting the first term to the purely rotational correction rigorously calculated by Bender *et al.* [23] on the basis of an exact projection of angular momentum; see also Refs. [24,25]. With the first term thus representing the rotational correction, the second term takes account of the *deformation dependence* of the vibrational correction [since E_{coll} as given by Eq. (3) vanishes for spherical nuclei we must suppose that the vibrational correction for such nuclei is absorbed into the fitted force parameters].

(iv) To the HFB energy calculated for the Skyrme and pairing forces we add a Wigner correction,

$$E_W = V_W \exp\left\{-\lambda\left(\frac{N-Z}{A}\right)^2\right\} + V_W'|N-Z|\exp\left\{-\left(\frac{A}{A_0}\right)^2\right\}, \tag{4}$$

which contributes significantly only for light nuclei ($A < A_0$) or nuclei with N close to Z. Our treatment of this correction is purely phenomenological, although physical interpretations of each of the two terms can be made [20,26].

(v) For an odd number of nucleons we adopt the equal-filling approximation [27].

(vi) We drop the Coulomb exchange term for protons. This is a device that leads to a significant improvement in the mass fits, especially mirror-nucleus differences, and it can be interpreted as simulating neglected effects such as Coulomb correlations, charge-symmetry breaking of the nuclear forces, and vacuum polarization [28].

III. THE NEW MASS MODELS

A. Fitting procedure

We use the CERN routine MINSQ to minimize the rms deviation of our models with respect to the mass data, but since there are 30 parameters in all (16 Skyrme parameters, five pairing parameters, four Wigner parameters, and five collective parameters) and there are 2353 masses to be fitted, some simplifying strategy has to be adopted. Since the four Wigner parameters are calculated separately we remove the 167 nuclei with $|N - Z| \leqslant 2$ from the data set and then of the remaining 2186 nuclei we take one third to form a fitting sample of 729 nuclei, chosen to ensure a mix of spherical, deformed, magic, light, heavy, even-even, odd-odd, and odd-A nuclei. Such a sample is found to be sufficiently representative, in the sense that taking a larger sample size will not change the rms error. On the other hand, we cannot take sample sizes that are significantly smaller without the rms error becoming sample dependent.

But even with the reduced data sets we cannot handle 26 parameters in the automatic minimization of the rms deviation with MINSQ. Furthermore, the minimization performed by numerical methods remains very sensitive to the initial starting point in the parameter space. For these reasons, of the 16 Skyrme parameters we preset t_2 at a value fixed on the basis of preliminary calculations, and adjust t_4, t_5, x_4, x_5, α, β, and γ manually, respecting the constraints of NeuM that we impose, along with the requirement that the incompressibility K_v fall within a certain narrow range of values. This leaves us with 8 Skyrme parameters for the automatic optimization but, as already explained, we impose fixed values on J and M_s^*. We likewise hold $k_{F0} = (3\pi^2 n_0/2)^{1/3}$ fixed at a constant value chosen for an optimal fit to charge radii, leaving us with five Skyrme degrees of freedom for automatic optimization. Of the five pairing parameters, ϵ_Λ and f_n^+ are, like t_2, preset at fixed values, while the remaining three parameters are included in the automatic minimization, which means that MINSQ is operated with eight degrees of freedom, the maximum that we found convenient (for a fitting sample of the size that we have taken), but also efficient enough to cover a large portion of the parameter space.

Most nuclei are, of course, deformed, and we have at our disposal both spherical and deformed HFB codes, both of which involve an expansion of the s.p. eigenstates on a harmonic-oscillator basis, as described in Refs. [29,30], but

TABLE II. Parameters of the new models of this paper; for convenience we also show model BSk21 [1]. Lines 1–16 show the Skyrme parameters, lines 17–21 the pairing parameters, and the last four lines the Wigner parameters (see text for further details). Note that it is more convenient to show the x_2 parameter in the form t_2x_2, the only combination in which x_2 enters into the formalism.

	BSk22	BSk23	BSk24	BSk25	BSk26	BSk21
t_0 [MeV fm^3]	−3978.97	−3974.58	−3970.29	−4068.39	−4072.53	−3961.39
t_1 [MeV fm^5]	404.461	400.199	395.766	431.093	439.536	396.131
t_2 [MeV fm^5]	0	0	0	0	0	0
t_3 [MeV fm$^{3+3\alpha}$]	22704.7	22676.3	22648.6	23342.8	23369.1	22588.2
t_4 [MeV fm$^{5+3\beta}$]	−100.000	−100.000	−100.000	−200.000	−100.0	−100.000
t_5 [MeV fm$^{5+3\gamma}$]	−150.000	−150.000	−150.000	−150.000	−120.0	−150.000
x_0	0.472558	0.673839	0.894371	1.20467	0.577367	0.885231
x_1	0.0627540	0.0609759	0.0563535	0.111366	−0.404961	0.0648452
t_2x_2 [MeV fm^5]	−1396.13	−1392.94	−1389.61	−1387.47	−1147.70	−1390.38
x_3	0.514386	0.770751	1.05119	1.44777	0.624831	1.03928
x_4	2.00000	2.00000	2.00000	2.00000	−3.00000	2.00000
x_5	−11.0000	−11.0000	−11.0000	−11.0000	−11.0000	−11.0000
α	1/12	1/12	1/12	1/12	1/12	1/12
β	1/2	1/2	1/2	1/2	1/6	1/2
γ	1/12	1/12	1/12	1/12	1/12	1/12
W_0 [MeV fm^5]	111.109	109.950	108.405	108.641	110.509	109.622
f_n^+	1.00	1.00	1.00	1.00	1.00	1.00
f_n^-	1.05	1.05	1.06	1.05	1.05	1.05
f_p^+	1.07	1.07	1.09	1.07	1.10	1.07
f_p^-	1.13	1.13	1.16	1.13	1.17	1.13
ε_Λ [MeV]	16.0	16.0	16.0	16.0	16.0	16.0
V_W [MeV]	−2.00	−1.80	−1.70	−1.60	−1.80	−1.80
λ	290	430	470	450	380	280
V'_W [MeV]	0.90	0.84	0.90	1.02	0.84	0.96
A_0	28	28	26	22	26	24

the overall computation time is reduced by more than an order of magnitude by performing the actual automatic fitting with just the spherical code, following a procedure developed by Tondeur *et al.* [31]. First, taking the latest available set of Skyrme, pairing and collective parameters we make a full (unconstrained) deformed-HFB calculation of the energy $E_{\rm eq}$ of each of the 729 nuclei in the fitting sample. Each of these calculations is then repeated with the deformed code constrained to the spherical configuration, the resulting energy being denoted by $E_{\rm sph}$. We can thus define for each nucleus a deformation energy $E_{\rm def} = E_{\rm sph} - E_{\rm eq}$, which is much less sensitive to the dimensionality of the code than is either of the two absolute energies $E_{\rm eq}$ and $E_{\rm sph}$. It is thus possible for the deformed code to have a lower dimensionality than would otherwise be the case; we found 21 major shells to be sufficient. These deformation energies $E_{\rm def}$ are then used to define an "equivalent spherical" experimental mass $E_{\rm exp}^{\rm sph} = E_{\rm exp} + E_{\rm def}$, which constitutes the pseudodata to be fitted by MINSQ with the HFB spherical code, for which we took a dimensionality of 20 major shells. When this automatic fit is finished a manual adjustment of the seven Skyrme parameters that were not fitted automatically by MINSQ is performed on the 729 nuclei of the fitting sample, and with this new set of parameters a new automatic minimization is started. This process is reiterated until the rms deviation for the reduced set of nuclear masses has fallen as far as is consistent with the other constraints that we have applied, as described in the foregoing.

At this point the performance of the current set of model parameters on the full data set of 2353 nuclei has to be tested. In general, the deformed code must be used, but since this has sufficient dimensionality to calculate only $E_{\rm def}$ with the required accuracy the spherical code must be used as well, the final energy of each nucleus being given by $E = E_0 - E_{\rm def}$, where E_0 is the energy given by the spherical code and $E_{\rm def}$ is calculated as already described. Both E_0 and $E_{\rm def}$ are calculated for each of the 2353 nuclei, and to the total energy E so determined has to be added the Wigner correction given by Eq. (4). In fitting the four Wigner parameters to the mass data we simultaneously retune (for the first time) the five parameters of the collective correction (3), minimizing the rms error on the 2353 experimental masses. Actually, of the five collective parameters, b and c have already been fixed, as described in the previous section, while the parameters l and β_2^0 are only poorly determined by masses. (The full generality of the second term in Eq. (3) is required only for fitting shape isomers and fission barriers [25].)

The entire procedure that we have described in this subsection is then reiterated in search of further improvement.

B. The mass fits

In fitting to the new data set of 2353 nuclei we generate in all five new sets of the Skyrme, pairing, and Wigner parameters, BSk22 to BSk26, along with the corresponding mass tables,

TABLE III. Parameters of Eq. (3) for collective correction.

	HFB-22	HFB-23	HFB-24	HFB-25	HFB-26
b (MeV)	0.80	0.80	0.80	0.80	0.80
c	10	10	10	10	10
d (MeV)	3.8	3.8	3.8	3.7	3.4
l	17	17	16	17	15
β_2^0	0.1	0.1	0.1	0.1	0.1

TABLE IV. rms (σ) and mean ($\bar{\epsilon}$) deviations between data and predictions for models of this paper. The first pair of lines refers to all the 2353 measured masses M that were fitted [19], the second pair to the masses M_{nr} of the subset of 257 neutron-rich nuclei with neutron separation energy $S_n \leqslant 5.0$ MeV, the third pair to the neutron separation energies S_n (2199 measured values), the fourth pair to β-decay energies Q_β (2065 measured values), and the fifth pair to charge radii (884 measured values [6]).

	HFB-22	HFB-23	HFB-24	HFB-25	HFB-26
$\sigma(M)$ [MeV]	0.629	0.569	0.549	0.544	0.564
$\bar{\epsilon}(M)$ [MeV]	−0.043	−0.022	−0.012	0.008	0.006
$\sigma(M_{nr})$ [MeV]	0.817	0.721	0.702	0.791	0.749
$\bar{\epsilon}(M_{nr})$ [MeV]	0.221	0.090	0.011	0.023	0.230
$\sigma(S_n)$ [MeV]	0.488	0.467	0.474	0.452	0.456
$\bar{\epsilon}(S_n)$ [MeV]	−0.018	−0.012	−0.009	−0.011	−0.015
$\sigma(Q_\beta)$ [MeV]	0.619	0.578	0.567	0.543	0.583
$\bar{\epsilon}(Q_\beta)$ [MeV]	0.026	0.013	0.010	0.015	0.021
$\sigma(R_c)$ [fm]	0.026	0.026	0.026	0.025	0.027
$\bar{\epsilon}(R_c)$ [fm]	0.002	0.00	−0.001	0.00	0.001

labeled HFB-22 to HFB-26, respectively. BSk22 to BSk25 are fitted to $J = 32$, 31, 30, and 29 MeV, respectively, and are all constrained to LS2, while BSk26 is fitted to $J = 30$ MeV under the APR constraint. In applying the NeuM constraints we make sure that over the full range of densities relevant to neutron stars there is no unphysical ferromagnetic flip to a polarized configuration.

The values of the parameters for these five new fits are shown in Table II. The parameters of the collective correction of Eq. (3) are shown in Table III. Figure 1 shows how well each of our five new models reproduces its "target" EOS of NeuM up to core densities. In this figure we supplement the "data" points representing the results of the realistic calculations of Refs. [3, 4] (in the case of Ref. [4] the "data" points were kindly supplied by H.-J. Schulze) by the constraints recently obtained from auxiliary field diffusion Monte Carlo calculations of Gandolfi *et al*. [32]. For comparison, we also show the very stiff EOS of Ref. [4] obtained from BHF calculations using the Bonn-B potential labeled "BOB" in Ref. [4] and which we refer to as LS3. Figure 2 is a zoom of Fig. 1 over the range of densities relevant to nuclei. The left panel shows the four models BSk22, BSk23, BSk24, and BSk25, all of which have been constrained by the high-density LS2 EOS, but each with a different value of J. The right panel compares models BSk24 and BSk26, which are constrained by the high-density LS2 and APR EOSs, respectively, but with $J = 30$ MeV in both cases. Both zooms show not only the constraints of Ref. [32] but also those obtained by Tews *et al*. [33] at next-to-next-to-next-to-leading order in chiral effective field theory. It is to be noted that all the "data" points of Refs. [3,4] fall within the domain delimited by these two sets of constraints. Moreover, it will be seen that of all our five models, only BSk25 fails to conform to one of the other of these constraints, having too high an energy. It should be realized that in constraining the Skyrme forces to one or the other of the realistic EOSs of NeuM we concentrated on supernuclear densities.

The rms and mean (data-theory) values of the deviations between the measured masses and the predictions for the five new models are given in the first and second lines, respectively, of Table IV. The next two lines of this table show the corresponding deviations for the subset consisting of the most neutron-rich measured nuclei, here taken as those with a neutron separation energy $S_n \leqslant 5.0$ MeV (there are 257 nuclei in this subset). All five models display, not surprisingly, some deterioration as we move into the neutron-rich region. From the first line we see that the parameter sets BSk24 ($J = 30$ MeV) and BSk25 ($J = 29$ MeV) give the best global fits of all the new models, and in fact are better than any of our previous models (see also Fig. 3). However, line 3 of Table IV shows that the deterioration of BSk25 on moving into the neutron-rich region

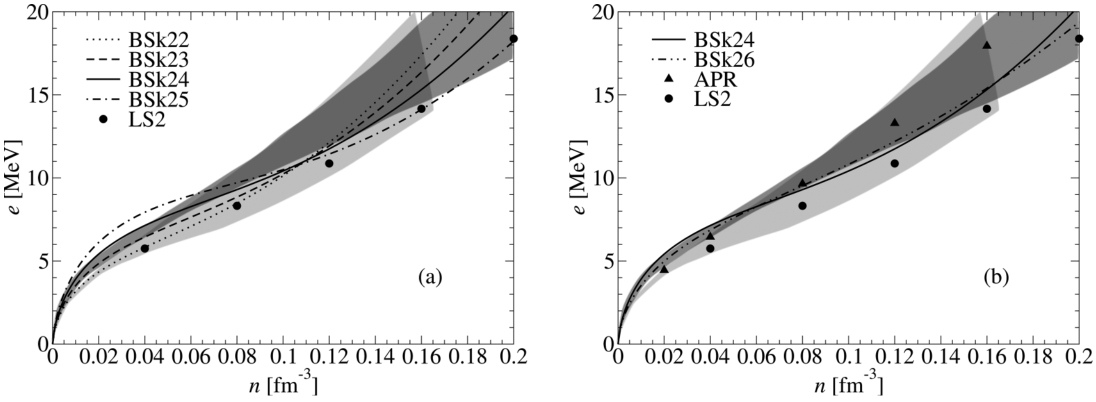

FIG. 2. Low-density zero-temperature EOS in neutron matter for models BSk22–26. The shaded areas represent the constraints of Ref. [32] (dark) and of Ref. [33] (light). Also shown are the realistic EOSs APR [3] and LS2 [4]. (a) only the Skyrme EOSs constrained to LS2 at high density are shown. (b) only the two Skyrme EOSs fitted to the same value of the symmetry coefficient are shown, namely $J = 30$ MeV.

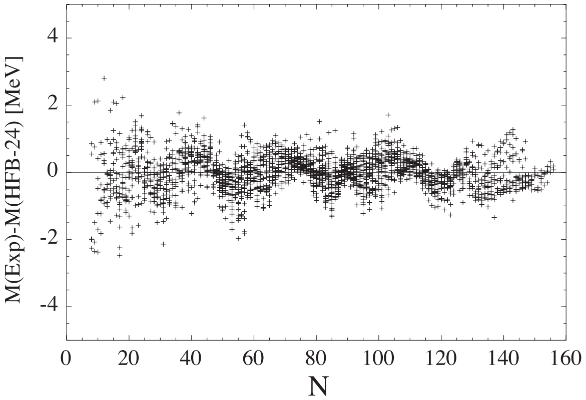

FIG. 3. Comparison between experimental and HFB-24 masses.

is much stronger than for BSk24: for all the other models the performance in the neutron-rich region correlates fairly well with the global performance. This may be related to the abnormal behavior of BSk25 in NeuM at subnuclear densities noted in connection with Fig. 2, but in any case it means that the apparent high performance of this model should be interpreted with caution. Looking at BSk22 and BSk23, we see from both lines 1 and 3 that $J = 31$ MeV works less well than either 29 or 30 MeV, while $J = 32$ MeV is still more strongly disfavored.

Lines 5–8 of Table IV show the deviations for the S_n and β-decay energies Q_β of all measured nuclei; these differential quantities are of greater astrophysical relevance than the absolute masses, both for the r-process and the crust of neutron stars. It will be seen that all models fit the S_n better than they fit the absolute masses, while most models fit the Q_β worse. BSk25 ($J = 29$ MeV) performs best for both S_n and Q_β, with the $J = 30$ and 31 MeV models following in no unambiguous order. Again, BSk22 ($J = 32$ MeV) is the worst performer in both the S_n and Q_β categories.

Comparing BSk24 and BSk26 shows that for $J = 30$ MeV the high-density LS2 constraint (BSk24) gives better fits than APR (BSk26) in all but one of the four categories. This is compatible with our observation in Sec. I that BSk21 performed better than BSk20 when run with the data of the 2012 AME.

Overall, the clearest conclusion that can be drawn from Table IV is that model BSk22 is the worst performing of all our models, ruling out $J = 32$ MeV. There are also very strong indications that $J = 29$ or 30 MeV (the latter in both its LS2 and APR forms) are to be preferred to $J = 31$ MeV, although we have already expressed some concerns with regards to $J = 29$ MeV, i.e., to BSk25.

The last two lines of Table IV show that all models give essentially identical high-quality fits to the charge-radius data, as shown in Fig. 4 for HFB-24 predictions. Similarly, an accurate prediction of the charge density of ^{208}Pb is found, as illustrated in the right panel of Fig. 4.

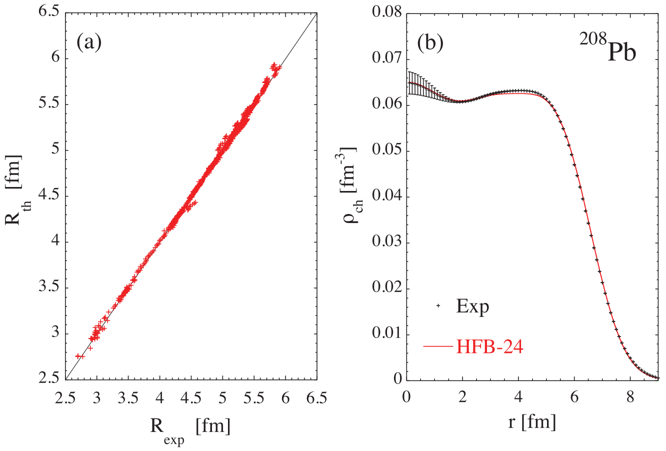

FIG. 4. (Color online) (a) HFB-24 charge radii versus experimental data [6]. (b) Comparison of the measured charge density [34] with HFB-24 estimate for ^{208}Pb.

C. Properties of infinite nuclear matter

All parameters appearing in Table V, except $\widetilde{L}$ and $\widetilde{K}_{\rm sym}$, are as defined in Ref. [1]. In particular, the first seven parameters are defined by first writing the energy per nucleon of INM of density n and charge asymmetry $\eta = (n_n - n_p)/n$ in the form

$$e(n,\eta) = e(n,\eta=0) + e_{\rm sym}^{(1)}(n)\eta^2 + O(\eta^4), \tag{5}$$

in which the first term on the right-hand side is just the energy per nucleon of charge-symmetric INM; we have neglected charge-symmetry breaking terms, such as those arising from the neutron-proton mass difference. We then expand $e(n,\eta = 0)$ and $e_{\rm sym}^{(1)}(n)$ about the equilibrium density n_0 in powers of $\epsilon = (n - n_0)/n_0$, thus

$$e(n,\eta=0) = a_v + \frac{1}{18}K_v\epsilon^2 - \frac{1}{162}K'\epsilon^3 + \cdots \tag{6a}$$

and

$$e_{\rm sym}^{(1)}(n) = J + \frac{1}{3}L\epsilon + \frac{1}{18}K_{\rm sym}\epsilon^2 + \cdots, \tag{6b}$$

in which

$$L = 3n_0\left(\frac{de_{\rm sym}^{(1)}(n)}{dn}\right)_{n=n_0} \tag{7a}$$

TABLE V. Parameters of infinite nuclear matter for models of this paper.

	BSk22	BSk23	BSk24	BSk25	BSk26
a_v [MeV]	−16.088	−16.068	−16.048	−16.032	−16.064
n_0 [fm^{-3}]	0.1578	0.1578	0.1578	0.1587	0.1589
J [MeV]	32.0	31.0	30.0	29.0	30.0
L [MeV]	68.5	57.8	46.4	36.9	37.5
$K_{\rm sym}$[MeV]	13.0	−11.3	−37.6	−28.5	−135.6
K_v [MeV]	245.9	245.7	245.5	236.0	240.8
K' [MeV]	275.5	275.0	274.5	316.5	282.9
$\widetilde{L}$ [MeV]	71.7	60.9	49.5	39.2	42.2
$\widetilde{K}_{\rm sym}$ [MeV]	12.6	−11.8	−38.2	−32.7	−130.3
M_s^*/M	0.80	0.80	0.80	0.80	0.80
M_v^*/M	0.71	0.71	0.71	0.74	0.65

and

$$K_{\rm sym} = 9n_0^2\left(\frac{d^{\,2}e_{\rm sym}^{(1)}(n)}{dn^2}\right)_{n=n_0}. \tag{7b}$$

1. Correlations among J, L, and $K_{\rm sym}$

Although we have concluded that J must have a value close to 29 or 30 MeV, with 32 MeV definitely excluded, it is still of interest to see what happens to L and $K_{\rm sym}$ when we vary J over the full range of 29 to 32 MeV. Table V shows that in our models L is strongly correlated with J, confirming what has been affirmed many times in the past; see, for example, Refs. [35–41].

It has also been suggested [42] that $K_{\rm sym}$ is correlated with L (and thus with J). However, we see from Table V that the situation with our forces is somewhat more complex. In particular, the value of $K_{\rm sym}$ is much more sensitive to the constraining EOS than to the corresponding values of L (or J): for models BSk22,BSk23, BSk24, and BSk25, all of which are constrained to the LS2 EOS, $K_{\rm sym}$ is considerably larger than for the BSk26 model, which is constrained to the softer EOS of APR. Clearly, a determination of L will not suffice to determine $K_{\rm sym}$, contrary to the assertion of Ref. [42].

In stressing the role of the constraining EOS on any possible correlation between J, L, and $K_{\rm sym}$, it should be recalled that it is the EOS of NeuM that is involved, and that because of the terms $O(\eta^4)$ in Eq. (5), the energy per nucleon of NeuM $e(n,\eta=1)$ is not given exactly by $e(n,\eta=0)+e_{\rm sym}^{(1)}(n)$. Rather, we should introduce, as in Ref. [1], a second symmetry energy defined in terms of NeuM, thus

$$e_{\rm sym}^{(2)}(n) = e(n,\eta=1) - e(n,\eta=0). \tag{8}$$

This can then be expanded about the density n_0 according to

$$e_{\rm sym}^{(2)}(n) = \widetilde{J} + \tfrac{1}{3}\widetilde{L}\epsilon + \tfrac{1}{18}\widetilde{K}_{\rm sym}\epsilon^2 + \cdots, \tag{9}$$

where

$$\widetilde{J} = e(n_0,\eta=1) - a_v, \tag{10a}$$

$$\widetilde{L} = 3n_0\left(\frac{de_{\rm sym}^{(2)}(n)}{dn}\right)_{n=n_0}, \tag{10b}$$

and

$$\widetilde{K}_{\rm sym} = 9n_0^2\left(\frac{d^{\,2}e_{\rm sym}^{(2)}(n)}{dn^2}\right)_{n=n_0}. \tag{10c}$$

Then the variation of the energy per neutron of NeuM with respect to density in the region of n_0 can be written as

$$\begin{aligned} e(n,\eta=1) &= e(n,\eta=0) + e_{\rm sym}^{(2)}(n) \\ &= e(n_0,\eta=1) + \tfrac{1}{3}\widetilde{L}\epsilon + \tfrac{1}{18}(K_v + \widetilde{K}_{\rm sym})\epsilon^2. \end{aligned} \tag{11}$$

It will be seen here that the second derivative of the NeuM curve is determined by the combination $K_v + \widetilde{K}_{\rm sym}$, rather than by just $\widetilde{K}_{\rm sym}$. It is only because the models presented here all lead to a K_v close to the experimental value that $\widetilde{K}_{\rm sym}$ takes more or less the same value for all those models that have been constrained by the same EOS of NeuM.

We have not used these quantities $\widetilde{L}$ and $\widetilde{K}_{\rm sym}$ before but for generalized Skyrme forces of the form (1) it follows from Eq. (A26) of Ref. [9] that

$$\begin{aligned} \widetilde{L} = {} & \frac{3\hbar^2}{5M_n}k_{Fn0}^2 + \frac{3}{4}t_0(1-x_0)n_0 + \frac{3}{8}[t_1(1-x_1) \\ & + 3t_2(1+x_2)]n_0\,k_{Fn0}^2 + \frac{1}{8}(\alpha+1)t_3(1-x_3)n_0^{\alpha+1} \\ & + \frac{3}{40}(3\beta+5)t_4(1-x_4)n_0^{\beta+1}\,k_{Fn0}^2 \\ & + \frac{9}{40}(3\gamma+5)t_5(1+x_5)n_0^{\gamma+1}\,k_{Fn0}^2 \end{aligned} \tag{12a}$$

and

$$\begin{aligned} \widetilde{K}_{\rm sym} = {} & -\frac{3\hbar^2}{5M}k_{Fn0}^2 + \frac{3}{4}[t_1(1-x_1) + 3t_2(1+x_2)]n_0\,k_{Fn0}^2 \\ & + \frac{3}{8}(\alpha+1)\alpha\, t_3(1-x_3)n_0^{\alpha+1} \\ & + \frac{3}{40}(3\beta+5)(3\beta+2)t_4(1-x_4)n_0^{\beta+1}\,k_{Fn0}^2 \\ & + \frac{9}{40}(3\gamma+5)(3\gamma+2)t_5(1+x_5)n_0^{\gamma+1}\,k_{Fn0}^2 - K_v, \end{aligned} \tag{12b}$$

where

$$k_{Fn0} = (3\pi^2 n_0)^{1/3}. \tag{13}$$

The eighth and ninth lines of Table V show the values of $\widetilde{L}$ and $\widetilde{K}_{\rm sym}$, respectively, for the models of this paper; it will be seen that they are not exactly equal to the corresponding values of L and $K_{\rm sym}$ [the difference arises from the terms $O(\eta^4)$ in Eq. (5)], but are closely correlated with them, so that L and $K_{\rm sym}$ can indeed serve as meaningful measures of the slopes and second derivatives of the NeuM curves at density n_0.

If we look now at the values of L for the first five models, all of which have been constrained to LS2, we see an almost linear correlation with J. This correlation can easily be understood from Eq. (5): since ϵ is negative over most of the nucleus, an increase in J must be accompanied by an increase of L, regardless of any constraining EOS. Since an increase of L implies an increase of $\widetilde{L}$, it follows that the fit of our Skyrme forces to the constraining EOS of NeuM, if ever exact for one value of J, cannot remain exact as J changes, given that $\widetilde{L}$ takes a fixed value for a given constraining EOS. Nevertheless, the value of $\widetilde{L}$ for the constraining EOS must have some impact on the model L, which means that if the constraining EOS is changed then L must change even if J remains unchanged. This explains why L takes different values for models BSk24 and BSk26, even though J is the same in both cases. However the impact of a change in the constraining EOS on the value of L is small, since it is the mass fits that determine primarily the value of L for a given J. On the other hand, nuclear masses are relatively insensitive to $K_{\rm sym}$, which explains why the value of $K_{\rm sym}$ is determined almost entirely by the constraining EOS, through its value of $\widetilde{K}_{\rm sym}$.

2. Effective masses

The values of the isoscalar and isovector effective masses, M_s^* and M_v^*, respectively, shown in Table V, are calculated at the equilibrium density n_0 of charge-symmetric INM. The value $M_s^* = 0.8M$ for all the models was, as already explained, a constraint imposed on the fit to the data, but the various values of M_v^* were left free and emerged from the fit. Experimental estimates of this quantity vary widely: measurements of the isovector giant dipole resonance (IVGDR) in heavy nuclei, as summarized in Fig. 47 of Ref. [43], indicate that the value of M_v^*/M can range from 0.7 to 1 (this figure in effect plots M/M_v^*). However, the subsequent discussion in Ref. [43] points out that lower values are possible, which means that none of our models is in clear conflict with experiment. Moreover, all five models have $M_v^* < M_s^*$, which implies that the neutron effective mass M_n^* is larger than the proton effective mass M_p^* in neutron-rich matter, since the effective mass of a nucleon of charge type q in nuclear matter at density n is given by

$$\frac{M}{M_q^*} = \frac{2n_q}{n}\frac{M}{M_s^*} + \left(1 - \frac{2n_q}{n}\right)\frac{M}{M_v^*}. \tag{14}$$

This prediction is consistent with measurements of the IVGDR [44], and has been confirmed in many-body calculations with realistic forces [45]. With these latter calculations giving $M_s^* = 0.825M$ and $M_v^* = 0.727M$, we see that the magnitude of the splitting given by the new models is quite realistic.

Figure 5 shows for the five new models how M_s^* and M_v^* vary with density. $1/M_s^*$ and $1/M_v^*$ vary nonlinearly with density for all these models, essentially because of the terms in t_4 and t_5. However, for all models but BSk25 the variation of M_s^* and M_v^* with density is monotonic almost everywhere, in accordance with many-body calculations using realistic two- and three-nucleon forces [2,45,46]. Actually, some nonmonotonicity, visible in Fig. 5 in the form of very weak peaks in the case of M_s^*, occurs at very low densities, but is of no direct physical interest, since at such densities INM is unstable. But in the case of model BSk25 the nonmonotonicity is pronounced and occurs at densities where INM is stable. This is one further respect in which BSk25 shows abnormal behavior.

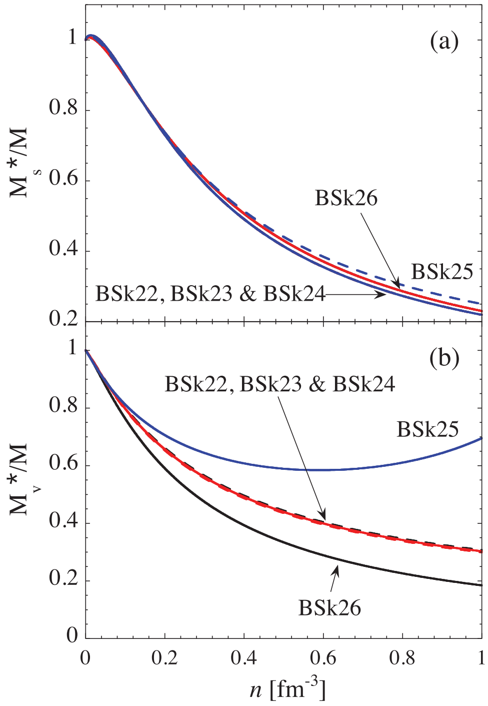

FIG. 5. (Color online) Variation with density of (a) M_s^*/M and (b) M_v^*/M.

3. Distribution of potential energy among the (S, T) channels

Fitting our forces to the mass data and the EOS of NeuM is not a sufficient condition for ensuring a realistic distribution of the potential energy per nucleon among the four two-body spin-isospin (S, T) channels in charge-symmetric INM. Figure 6 shows this distribution for each of our five new forces as a function of density, and compares with two different BHF calculations: "Catania 1" based on Ref. [4] and "Catania 2" based on Ref. [47]. Given the evident uncertainty in what the real distribution actually is, the level of agreement we have found with our new forces can be regarded as satisfactory. This would have been very difficult within the framework of conventional Skyrme forces and the term in t_5 has been indispensable in this respect (see the discussion in Ref. [44]). The importance of a realistic distribution of the potential energy among the (S, T) channels for deformation energy was discussed long ago in Refs. [48,49]. Deformation energy has also been shown to be sensitive to the surface-symmetry coefficient a_{ss} [50,51], an observation that opens up the possibility that a_{ss} is itself sensitive to the distribution of the potential energy among the (S, T) channels.

4. Constraints from heavy-ion collisions

We have calculated the pressure in charge-symmetric INM as a function of density for our forces and find that it is consistent with measurements of nuclear-matter flow and kaon production in heavy-ion collisions [11,12], although close to the upper limit, as shown in Fig. 7.

D. Neutron skins

For a given nucleus the neutron-skin thickness is defined by

$$\theta \equiv R_n^{\mathrm{rms}} - R_p^{\mathrm{rms}}, \tag{15}$$

where the rms radii refer to *point* nucleons. By considering the results of nonrelativistic Hartree-Fock and relativistic mean-field calculations with many different forces it was noted by Brown [52] and by Typel and Brown [53] that a strong correlation exists between the neutron-skin thickness and the value of the L coefficient. Thus, insofar as L and J are correlated (note that we have seen above that this correlation is somewhat weakened by our new models), it follows that the value of θ is likewise correlated with J: see,

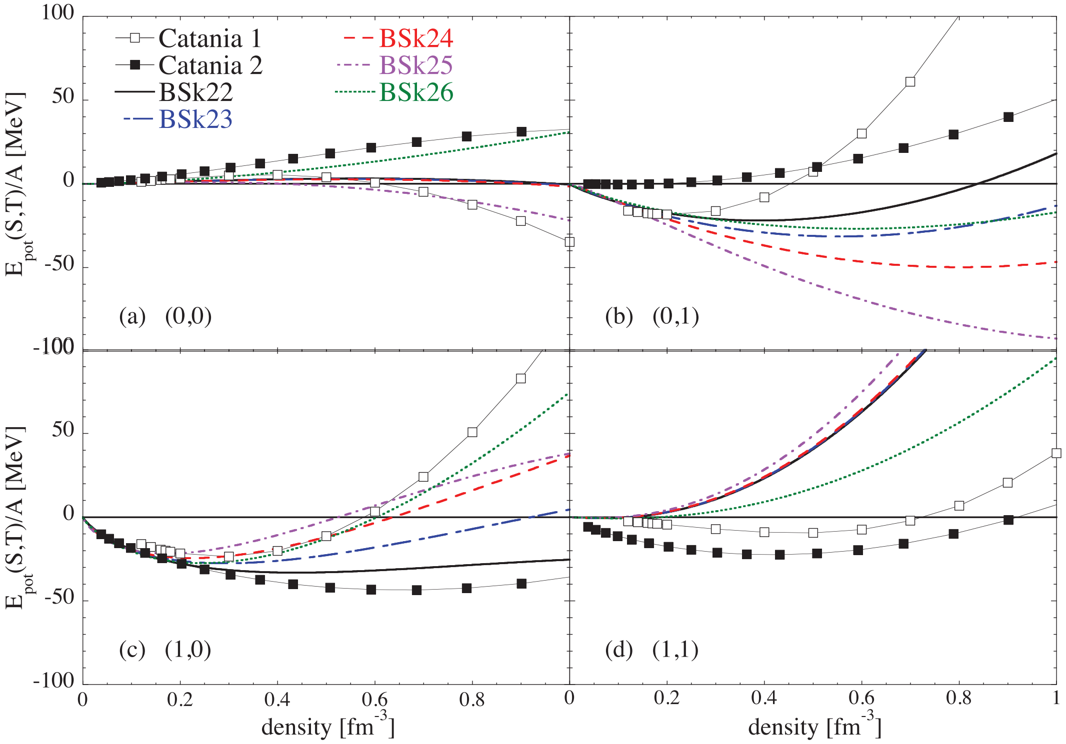

FIG. 6. (Color online) Potential energy per particle E_{pot}/A in each (S, T) channel as a function of density for charge-symmetric INM. The open symbols correspond to the "Catania 1" BHF calculations [4], and the solid symbols to the "Catania 2" BHF calculations [47].

for example, Table II of Ref. [36]. This correlation can easily be understood [24] in terms of the droplet-model expression (2.21) of Ref. [54] for the neutron-skin thickness of a nucleus of atomic number Z and mass number A,

$$\theta = \frac{3}{2} r_0 \frac{J}{Q} I, \qquad (16)$$

where $r_0 = (3/4\pi\, n_0)^{1/3}$, $I = (N - Z)/A$, and Q is the surface-stiffness coefficient, which is anticorrelated with J if masses are fitted [55,56]; see also Ref. [38] for a recent extensive discussion. (The fact that J is also correlated with L, as noted in Sec. III C, means that L and Q are anticorrelated. This is easy to understand, given that L measures the rate of variation of the energy per nucleon with respect to density over the surface, and assuming a local-density approximation.)

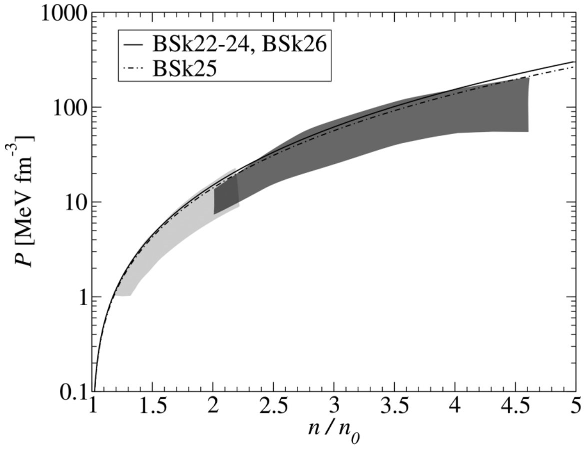

FIG. 7. Pressure as a function of density in charge-symmetric nuclear matter for our forces. The shaded area represents the analysis of heavy-ion collision experiments obtained in Refs. [11,12].

In Table VI we show the results of a set of measurements of θ on 26 nuclei using antiproton scattering [57]. The same table shows the results we calculate for these nuclei for each of our models. In Table VII we show the rms deviations σ_{rms} between our models and experiment, the mean deviations $\bar{\epsilon}$ and the model error σ_{mod} of Möller and Nix [58]. This last quantity provides a more reliable method of assessing the relative performance of different models, especially when the experimental errors are large, as in the present case (see also Appendix B of Ref. [59] for further comments). In the first three columns of this table we show the results for the full set of 26 nuclei, while in the next three columns we consider only the ten nuclei for which the experimental errors are 0.04 fm or less.

We see that all three deviations, for both the complete set of data and the subset, lead to the conclusion that models BSk24 and BSk26 are better than model BSk23. That is, $J = 30$ MeV is favored over $J = 31$ MeV. Likewise, BSk22 ($J = 32$ MeV) gives unambiguously the worst agreement with the measured skins (only in the case of BSk25, i.e., $J = 29$ MeV, is there any ambiguity). Thus there is almost complete agreement with the conclusions about J already drawn from the mass fits. On the other hand, these skin data are not precise enough to lead to any conclusions concerning the EOS of NeuM at nuclear densities.

Furthermore, we should exercise some caution in concluding that the skin data favor $J = 30$ MeV. A new analysis [60]

TABLE VI. Experimental and calculated neutron-skin thicknesses; data come from Ref. [57].

Z	A	Expt.	BSk22	BSk23	BSk24	BSk25	BSk26
20	40	$-0.08^{+0.05}_{-1.0}$	−0.05	−0.05	−0.05	−0.05	−0.05
20	48	$0.09^{+0.05}_{-0.05}$	0.17	0.16	0.15	0.14	0.15
26	54	$0.04^{+0.06}_{-0.08}$	−0.02	−0.02	−0.02	−0.03	−0.02
26	56	$0.03^{+0.08}_{-0.11}$	0.04	0.03	0.03	0.02	0.03
26	57	$0.07^{+0.05}_{-0.05}$	0.07	0.06	0.05	0.05	0.05
27	59	$0.00^{+0.08}_{-0.13}$	0.07	0.07	0.06	0.05	0.06
28	58	$-0.09^{+0.09}_{-0.16}$	0.00	−0.01	−0.01	−0.01	−0.02
28	60	$-0.01^{+0.08}_{-0.15}$	0.05	0.04	0.04	0.03	0.03
28	64	$0.04^{+0.07}_{-0.08}$	0.13	0.12	0.11	0.10	0.11
40	90	$0.09^{+0.02}_{-0.02}$	0.06	0.05	0.05	0.04	0.05
40	96	$0.12^{+0.03}_{-0.03}$	0.17	0.15	0.14	0.13	0.14
48	106	$0.10^{+0.10}_{-0.14}$	0.06	0.05	0.04	0.03	0.04
48	116	$0.15^{+0.04}_{-0.04}$	0.16	0.15	0.13	0.12	0.14
50	112	$0.07^{+0.02}_{-0.02}$	0.07	0.06	0.05	0.04	0.05
50	116	$0.10^{+0.03}_{-0.03}$	0.11	0.10	0.09	0.08	0.09
50	120	$0.08^{+0.03}_{-0.04}$	0.15	0.14	0.12	0.11	0.12
50	124	$0.14^{+0.03}_{-0.03}$	0.19	0.17	0.15	0.13	0.15
52	122	$0.08^{+0.04}_{-0.05}$	0.12	0.10	0.09	0.08	0.09
52	124	$0.06^{+0.04}_{-0.04}$	0.13	0.12	0.11	0.09	0.11
52	126	$0.11^{+0.03}_{-0.05}$	0.15	0.14	0.12	0.10	0.12
52	128	$0.11^{+0.04}_{-0.05}$	0.17	0.15	0.13	0.12	0.14
52	130	$0.15^{+0.06}_{-0.08}$	0.18	0.16	0.15	0.13	0.15
82	208	$0.15^{+0.02}_{-0.02}$	0.18	0.16	0.14	0.12	0.14
83	209	$0.18^{+0.04}_{-0.06}$	0.17	0.15	0.13	0.11	0.13
90	232	$0.21^{+0.07}_{-0.07}$	0.18	0.16	0.14	0.12	0.15
92	238	$0.21^{+0.07}_{-0.07}$	0.18	0.16	0.14	0.12	0.15

of the experiments of Ref. [57] suggests that the skin thickness of ^{208}Pb might be considerably larger than the value shown in Table VI. It is not clear to what extent the new analysis would apply to the other nuclei investigated in Ref. [57].

As for the PREX experiment on ^{208}Pb, a value of $0.33^{+0.16}_{-0.18}$ fm is quoted [61]; the lower limit of the error bars just includes the value of Ref. [57]. Other recent measurements are conveniently summarized in Ref. [62]. Probably the safest statement that we can make is that the neutron-skin data are not in any clear-cut conflict with the conclusions that we have drawn from nuclear masses.

TABLE VII. rms, mean, and model deviations between models of this paper and the experiments of Ref. [57]. The first three columns relate to the complete set of 26 nuclei, the last three columns to the set of ten nuclei with the lowest experimental error.

	σ_{rms} (26)	$\bar{\epsilon}$ (26)	σ_{mod} (26)	σ_{rms} (10)	$\bar{\epsilon}$ (10)	σ_{mod}(10)
BSk22	0.0495	−0.0266	0.0205	0.0429	−0.030	0.0244
BSk23	0.0447	−0.0142	0.0090	0.0342	−0.017	0.0128
BSk24	0.0437	−0.0031	0.0047	0.0270	−0.0030	0.0087
BSk25	0.0469	0.0088	0.0170	0.0277	0.011	0.0194
BSk26	0.0415	−0.0038	0.0044	0.0265	−0.0040	0.0084

E. Other estimates of the symmetry coefficient *J*

As far as we know, the only other attempts to extract a value of J from essentially all the available mass data are all based on one form or another of the liquid-drop model. The most recent such work is that of Möller *et al.* [63], who use their finite-range droplet model (FRDM) to find $J = 32.5 \pm 0.5$ MeV, a value which is quite incompatible with our own calculations, which favor a value in the range of 29–30 MeV. (Indeed, since Möller *et al.* take a prefixed value of $J = 35$ MeV in the microscopic part of their calculation, an even higher value might be expected to result from a more self-consistent calculation.) Möller *et al.* base their result on a fit to the 2149 measured masses of nuclei with N and $Z \geqslant 8$ given in the 2003 AME [13]; they do not quote any value for their rms deviation, but it must be larger than the 0.570 MeV that they quote for their model error [58] (in the case of our own models the rms deviation is about 0.008 MeV higher than the model deviation). On the other hand, Liu *et al.* [64], fit exactly the same data with a different form of the liquid-drop model, and find $J = 29.1$ MeV, the rms deviation being 0.336 MeV. Using a more restricted fit to the drop model, Royer *et al.* [65] find values of J ranging from 26.4 to 30.8 MeV. Yet another application of the liquid-drop model [66] yields $J = 31.3$ MeV or 32.1 MeV, according to the form chosen for the Wigner energy.

Clearly, a better understanding of the different forms of the liquid-drop model is required. The problem may lie in an inadequate parametrization of the surface-symmetry energy by the FRDM, as suggested many years ago, when it was shown that the droplet model fails to take account of the softening of the neutron skin at large neutron excesses that was predicted by more microscopic models [67]: the droplet is not only leptodermous but also malacodermous. Thus, when the standard FRDM is fitted to all the available data, the tendency will be for the surface-stiffness coefficient Q to adapt to the very neutron-rich data with a spuriously low value. But we have already pointed out the anticorrelation that masses impose between J and Q, so it is conceivable that an FRDM generalized to include higher-order surface-symmetry terms would lead to a lower value of J. As for Liu *et al.* [64], they do not consider surface symmetry at all, which means that they effectively have an infinite value of Q. Revising their model along the lines we have suggested could thus be expected to lead to a *higher* value of J.

All attempts other than our own to use mean-field methods to extract J from nuclear masses are based, to the best of our knowledge, on very limited data fields. For example, in a 2010 paper [68] the UNEDF (unified nuclear energy-density functional) project used 72 masses to arrive at a value of $J = 30.5$ MeV, a value that is quite consistent with our own results. However, more recently the UNEDF collaborators added seven nuclei (including four fission isomers) to their database [69], and found that J fell to 28.987 MeV, showing clearly thereby the need for a much larger data base. It is interesting to note that in both versions of UNEDF the EOS of NeuM is even softer at densities typical of neutron-star cores than that of FP [2], which itself is, as already noted, too soft to support the massive neutron stars PSR J1614−2230 and PSR J0348 + 0432. Now in Ref. [24] it was shown that releasing the constraint to a realistic EOS of NeuM will reduce the optimum value of J below 30 MeV, implying that similarly low values of J are to be expected with the UNEDF approach.

Also in the context of mean-field approaches, it is appropriate to mention the Skyrme model SLy4 [70], much used in neutron-star studies. It was fitted to just five nuclear masses, and gives $J = 32.0$ MeV. However, two of the five fitted masses have $N = Z$, but since there is no Wigner term these nuclei could only have been fitted by an excessive attraction in the isoscalar part of the force, which in turn would have to be compensated by an excessively large value of J if the three nuclei with $N \neq Z$ were to be fitted.

Using the full set of the mass data now available should provide a highly reliable basis for the determination of J, since it represents over 2300 precision measurements. However, other methods, conveniently summarized in Ref. [62], have also been used. For example, referring to their Fig. 2 we see that heavy-ion collisions establish limits on the $J - L$ correlation; all our models except BSk26 fall within these limits (when extrapolated to $J = 29$ MeV). Tighter limits on the $J - L$ correlation have been established in Refs. [40,41]; only BSk23 ($J = 31$ MeV) and BSk24 ($J = 30$ MeV) fall within these limits (along with BSk21, but not BSk19 or BSk20). Finally, we mention the very recent work of Roca-Maza *et al.* [71], who use measurements of the isovector giant quadrupole resonance to conclude that $L = 37 \pm 18$ MeV, which would eliminate BSk22 and BSk23, i.e., we must have $J \leqslant 30$ MeV.

F. Maximum mass of neutron stars

We complete Table I by calculating the maximum mass of neutron stars for each of the new models of this paper, solving the TOV equations. We assume that neutron stars are homogeneous throughout. That is, unlike our earlier calculations on BSk19, BSk20 and BSk21 [16], we neglect the inhomogeneities of the outer and inner crusts; we have verified by repeating the calculations of Ref. [16] that the impact of this approximation on the maximum mass is negligibly small. We see from Table I that all our new models are compatible with the existence of the massive neutron stars PSR J1614−2230 and PSR J0348 + 0432. Indeed, it turns out that the maximum mass is essentially the same for all models constrained by the same EOS of NeuM, in particular, it seems to be independent of the symmetry coefficient J.

G. Shell gaps

While we have seen that the global mass fit is rather accurate (Fig. 3), a few individual predictions could still be quite anomalous without having a serious impact on the global fit. Of particular importance in this respect are the masses involved in the definition of the neutron-shell gaps

$$\Delta_n(N_0, Z) = S_{2n}(N_0, Z) - S_{2n}(N_0 + 2, Z), \tag{17}$$

where S_{2n} is the two-neutron-separation energy; the proton-shell gaps can be similarly defined for a given proton number Z_0. We show in Fig. 8, the neutron-shell gaps for $N_0 = 28$, 50, 82, and 126 as well as the proton-shell gaps for $Z_0 = 50$

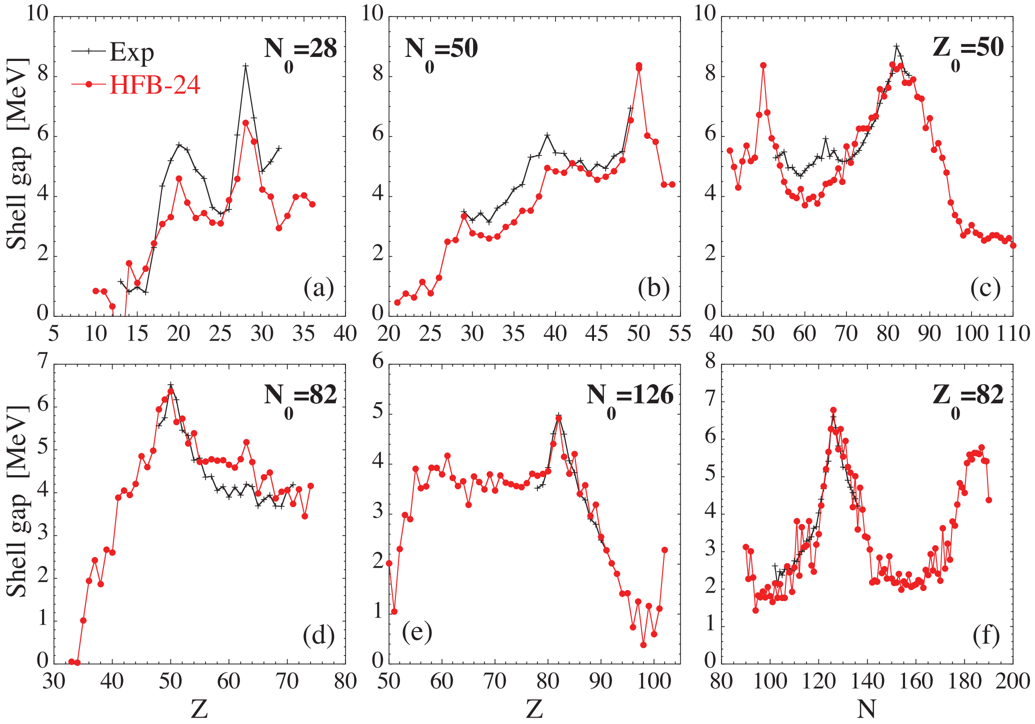

FIG. 8. (Color online) $N_0 = 28$ (a), 50 (b), 82 (d), and 126 (e) neutron-shell gaps as well as $Z_0 = 50$ (c) and 82 (f) proton-shell gaps for mass model HFB-24, as compared with experimental data

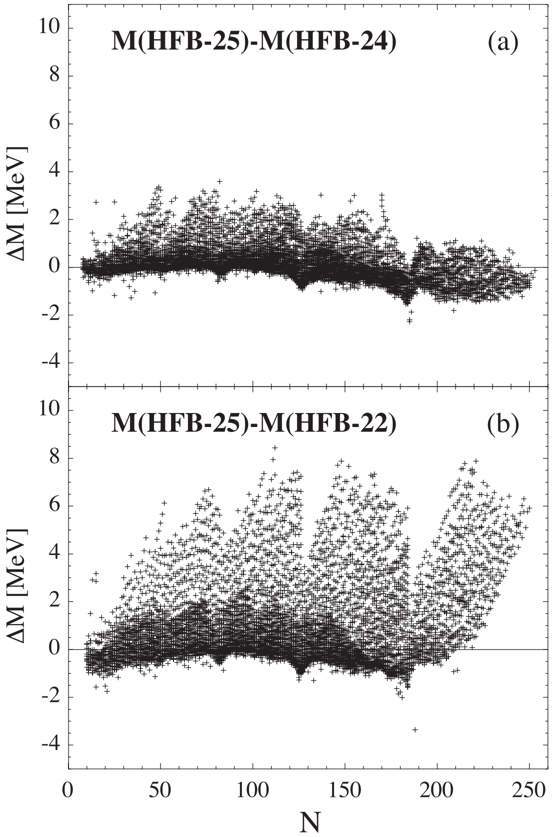

FIG. 9. (a) Differences between HFB-25 and HFB-24 mass predictions for all 8509 nuclei included in the tables. (b) Differences between HFB-25 and HFB-22 mass predictions

and 82. The agreement can be considered as excellent, for all magic numbers.

H. Extrapolation towards the neutron-drip line

Concerning the extrapolation of masses far away from experimental data, we show in Fig. 9, for all the nearly 8500 nuclei with $8 \leqslant Z \leqslant 110$ lying between the proton and neutron drip lines, the deviations between our two best-fit mass models, i.e HFB-24 and HFB-25, as well as between the two mass models with the largest difference in the symmetry coefficient, i.e., HFB-25 with $J = 29$ MeV and HFB-22 with $J = 32$ MeV. While in the first case, deviations are restricted to the narrow range of ±2 MeV, much larger discrepancies, up to 8 MeV, are found between HFB-25 and HFB-22. In addition, it is worth noting that the lower the J value the larger the masses predicted when approaching the neutron drip line.

This result is rather counter-intuitive, but a similar phenomenon was encountered in Ref. [24]. Referring to the discussion in that paper, and noting that the surface-symmetry coefficient is given by

$$a_{ss} = \frac{2a_{sf}L}{K_v} - \frac{9J^2}{4Q}, \tag{18}$$

we see that the phenomenon can be explained ultimately by the fact that the factor $(J + a_{ss}A^{-1/3})$ of I^2 appearing in the liquid-drop expression for the energy per nucleon, becomes smaller as J increases. In any case, it is precisely because of such deviations that new mass measurements in the far neutron-rich region help to tie down the symmetry coefficient.

IV. CONCLUSIONS

This paper describes the latest effort in our long-running project of developing HFB mass models that give precision fits to all the available mass data while at the same time respecting the constraints appropriate to the treatment of highly neutron-rich environments of astrophysical interest. The present paper extends our previous work by (a) refitting to the data of the 2012 AME [19], (b) varying the symmetry coefficient J over the range 29–32 MeV. Our models are characterized by unconventional Skyrme forces containing t_4 and t_5 terms, i.e., density-dependent generalizations of the usual t_1 and t_2 terms, respectively; they are constrained to fit one or the other of the APR and LS2 EOSs of NeuM, which are based on realistic two- and three-nucleon forces, and are stiff enough to support the massive neutron stars PSR J1614−2230 and PSR J0348 + 0432. At the same time, we are able to eliminate unphysical spin and spin-isospin instabilities of INM, including the transition to a polarized state in neutron-star matter. As for the contact pairing force, it is constrained to fit the gaps of INM of the appropriate density and charge asymmetry, as calculated with realistic two-nucleon and three-nucleon realistic forces.

Five new models, labeled BSk22 to BSk26, along with their mass tables, HFB-22 to HFB-26, respectively, are presented. The best fits to the new data base of 2353 nuclei are found for models BSk24 ($J = 30$ MeV) and BSk25 ($J = 29$ MeV), for which the rms deviations are 0.55 and 0.54 MeV, respectively. Despite the larger data base this is even better than the rms deviation of 0.58 MeV that we found with our fits to the 2003 AME. However, even though BSk25 gives a slightly better global fit than does BSk24, it deteriorates badly for highly neutron-rich nuclei, a problem that may be related to the relatively poor fit that it gives to NeuM at low densities; another abnormality that we have noted with BSk25 consists in the nonmonotonic variation of the effective mass with density. We thus regard model BSk24 as the more reliable. Since it has been fitted to $J = 30$ MeV and constrained to LS2, like BSk21, it may be regarded as an improved version of the latter; one sees from Table II that the parameters of the two forces are very similar. We might thus reasonably expect BSk24 to be as reliable as BSk21 in extrapolating to unknown regions of the nuclear chart: we have already pointed out the precision with which BSk21, fitted to the AME of 2003, predicted the new masses of the AME of 2012. But whether we take 29 or 30 MeV as the best value for J, we find that $J = 32$ MeV gives a significantly worse mass fit, the rms deviation rising to 0.63 MeV. This is in accord with UNEDF mean-field calculations performed on a much smaller data base, but is in conflict with the conclusions of the finite-range droplet model [63]. We have shown that the neutron-skin thicknesses derived from data on antiproton scattering [57] are likewise consistent with a value of J in the range 29–30 MeV.

The new mass data discriminate in favor of the LS2 EOS of NeuM over that of the slightly softer one of APR; using just the data of the 2003 AME it was impossible to distinguish between the two EOSs. It must be stressed, however, that this discrimination in favor of the LS2 EOS for NeuM relates only to nuclear and subnuclear densities. In particular, we should not conclude that nuclear masses are telling us something about the EOS of NeuM at the higher densities found in neutron-star cores, since it is conceivable that the Skyrme form (1) could be generalized still further in such a way that the EOS at high densities was changed without affecting the fit to nuclear masses.

As was the case with our models BSk19, BSk20, and BSk21, the new models are well adapted to a unified treatment of all parts of neutron stars: the outer crust [72], the inner crust [73], and the core [1]. The relevance of the models to the core of neutron stars arises not only from their fit to a sufficiently stiff EOS of NeuM but also from their fit to nuclear masses, which implies that they take correct account of the presence of protons. For the same reason these models take account of inhomogeneities, and thus are appropriate for the calculation of the inner crust of neutron stars. As for the outer crust, its properties are determined entirely by the mass tables that we have generated for the appropriate interactions. This is in contrast to the very recent Ref. [74], which does not generate mass tables and thus cannot handle the outer crust.

We have found that all our new models support the massive neutron stars PSR J1614−2230 and PSR J0348 + 0432; also that neutron-star masses cannot tell us anything about the symmetry coefficient J. We will discuss other implications of our new models for neutron stars in a separate paper.

ACKNOWLEDGMENTS

We wish to thank G. Audi, D. Lunney, and H.-J.Schulze for valuable communications. This work was financially supported by the FNRS (Belgium) and the NSERC (Canada).

[1] S. Goriely, N. Chamel, and J. M. Pearson, Phys. Rev. C **82**, 035804 (2010).
[2] B. Friedman and V. R. Pandharipande, Nucl. Phys. A **361**, 502 (1981).
[3] A. Akmal, V. R. Pandharipande, and D. G. Ravenhall, Phys. Rev. C **58**, 1804 (1998).
[4] Z. H. Li and H.-J. Schulze, Phys. Rev. C **78**, 028801 (2008).
[5] D. T. Loan, N. H. Tan, D. T. Khoa, and J. Margueron, Phys. Rev. C **83**, 065809 (2011).
[6] I. Angeli and K. P. Marinova, At. Data Nucl. Data Tables **99**, 69 (2013).
[7] S. Goriely, M. Samyn, M. Bender, and J. M. Pearson, Phys. Rev. C **68**, 054325 (2003).
[8] G. Colò, N. V. Giai, J. Meyer, K. Bennaceur, and P. Bonche, Phys. Rev. C **70**, 024307 (2004).
[9] N. Chamel, S. Goriely, and J. M. Pearson, Phys. Rev. C **80**, 065804 (2009).
[10] N. Chamel and S. Goriely, Phys. Rev. C **82**, 045804 (2010).
[11] P. Danielewicz, R. Lacey, and W. G. Lynch, Science **298**, 1592 (2002).
[12] Lynch *et al.*, Prog. Part. Nucl. Phys. **62**, 427 (2009).
[13] G. Audi, A. H. Wapstra, and C. Thibault, Nucl. Phys. A **729**, 337 (2003).
[14] P. B. Demorest, T. Pennucci, S. M. Ransom, M. S. E. Roberts, and J. W. T. Hessels, Nature **467**, 1081 (2010).
[15] J. Antoniadis *et al.*, Science **340**, 1233232 (2013).
[16] N. Chamel, A. F. Fantina, J. M. Pearson, and S. Goriely, Phys. Rev. C **84**, 062802 (2011).
[17] R. C. Tolman, Phys. Rev. **55**, 364 (1939).
[18] J. R. Oppenheimer and G. M. Volkoff, Phys. Rev. **55**, 374 (1939).
[19] G. Audi, M. Wang, A. H. Wapstra, F. G. Kondev, M. MacCormick, X. Xu, and B. Pfeiffer, Chinese Physics C **36**, 1287 (2012).
[20] N. Chamel, S. Goriely, and J. M. Pearson, Nucl. Phys. A **812**, 72 (2008).
[21] S. Goriely, N. Chamel, and J. M. Pearson, Phys. Rev. Lett. **102**, 152503 (2009).
[22] N. Chamel, Phys. Rev. C **82**, 014313 (2010).
[23] M. Bender, P.-H. Heenen, and P. Bonche, Phys. Rev. C **70**, 054304 (2004).
[24] S. Goriely, M. Samyn, J. M. Pearson, and M. Onsi, Nucl. Phys. A **750**, 425 (2005).
[25] S. Goriely, M. Samyn, and J. M. Pearson, Phys. Rev. C **75**, 064312 (2007).
[26] S. Goriely, M. Samyn, P.-H. Heenen, J. M. Pearson, and F. Tondeur, Phys. Rev. C **66**, 024326 (2002).
[27] S. Perez-Martin and L. M. Robledo, Phys. Rev. C **78**, 014304 (2008).
[28] S. Goriely and J. M. Pearson, Phys. Rev. C **77**, 031301(R) (2008).
[29] M. Samyn, S. Goriely, P.-H. Heenen, J. M. Pearson, and F. Tondeur, Nucl. Phys. A **700**, 142 (2002).
[30] M. Samyn, Ph.D. thesis, Université Libre de Bruxelles (2004).
[31] F. Tondeur, S. Goriely, J. M. Pearson, and M. Onsi, Phys. Rev. C **62**, 024308 (2000).
[32] S. Gandolfi, J. Carlson, and S. Reddy, Phys. Rev. C **85**, 032801(R) (2012).
[33] I. Tews, T. Krüger, K. Hebeler, and A. Schwenk, Phys. Rev. Lett. **110**, 032504 (2013).
[34] H. Euteneuer, J. Friedrich, and N. Voegler, Nucl. Phys. A **298**, 452 (1978).
[35] M. Farine, J. M. Pearson, and B. Rouben, Nucl. Phys. A **304**, 317 (1978).
[36] F. Tondeur, M. Brack, M. Farine, and J. M. Pearson, Nucl. Phys. A **420**, 297 (1984).
[37] P.-G. Reinhard, Nucl. Phys. A **649**, 305c (1999).
[38] M. Warda, X. Viñas, X. Roca-Maza, and M. Centelles, Phys. Rev. C **80**, 024316 (2009).
[39] P.-G. Reinhard and W. Nazarewicz, Phys. Rev. C **81**, 051303(R) (2010).
[40] J. M. Lattimer and Y. Lim, Astrophys. J. **771**, 51 (2013).
[41] J. M. Lattimer, Annu. Rev. Nucl. Part. Sci. **62**, 485 (2012).
[42] J. Dong, W. Zuo, J. Gu, and U. Lombardo, Phys. Rev. C **85**, 034308 (2012).

[43] B. L. Berman and S. C. Fultz, Rev. Mod. Phys. **47**, 713 (1975).

[44] T. Lesinski, K. Bennaceur, T. Duguet, and J. Meyer, Phys. Rev. C **74**, 044315 (2006).

[45] L. G. Cao, U. Lombardo, C. W. Shen, and Nguyen V. Giai, Phys. Rev. C **73**, 014313 (2006).

[46] W. Zuo, I. Bombaci, and U. Lombardo, Phys. Rev. C **60**, 024605 (1999).

[47] X. R. Zhou, G. F. Burgio, U. Lombardo, H.-J. Schulze, and W. Zuo, Phys. Rev. C **69**, 018801 (2004).

[48] A. B. Volkov, Nucl. Phys. A **141**, 337 (1970).

[49] G. Saunier, B. Rouben, and J. M. Pearson, Phys. Lett. B **48**, 293 (1974).

[50] F. Tondeur, Nucl. Phys. A **442**, 460 (1985).

[51] N. Nikolov, N. Schunck, W. Nazarewicz, M. Bender, and J. Pei, Phys. Rev. C **83**, 034305 (2011).

[52] B. A. Brown, Phys. Rev. Lett. **85**, 5296 (2000).

[53] S. Typel and B. A. Brown, Phys. Rev. C **64**, 027302 (2001).

[54] W. D. Myers and W. J. Swiatecki, Ann. Phys. (NY) **55**, 395 (1969).

[55] M. Farine, J. Côté, and J. M. Pearson, Nucl. Phys. A **338**, 86 (1980).

[56] M. Farine, J. Cônté, and J. M. Pearson, Phys. Rev. C **24**, 303 (1981).

[57] J. Jastrzębski, A. Trzcińska, P. Lubiński, B. Klos, F. J. Hartmann, T. von Egidy, and S. Wycech, Int. J. Mod. Phys. E **13**, 343 (2004).

[58] P. Möller and J. R. Nix, At. Data Nucl. Data Tables **39**, 213 (1988).

[59] D. Lunney, J. M. Pearson, and C. Thibault, Rev. Mod. Phys. **75**, 1021 (2003).

[60] B. A. Brown, G. Shen, G. C. Hillhouse, J. Meng, and A. Trzcińska, Phys. Rev. C **76**, 034305 (2007).

[61] S. Abrahamyan *et al.*, Phys. Rev. Lett. **108**, 112502 (2012).

[62] M. B. Tsang *et al.*, Phys. Rev. C **86**, 015803 (2012).

[63] P. Möller, W. D. Myers, H. Sagawa, and S. Yoshida, Phys. Rev. Lett. **108**, 052501 (2012).

[64] M. Liu, N. Wang, Y. Deng, and X. Wu, Phys. Rev. C **84**, 014333 (2011).

[65] G. Royer, M. Guilbaud, and A. Onillon, Nucl. Phys. A **847**, 24 (2010).

[66] H. Jiang, G. J. Fu, Y. M. Zhao, and A. Arima, Phys. Rev. C **85**, 024301 (2012).

[67] A. K. Dutta, J.-P. Arcoragi, J. M. Pearson, R. H. Behrman, and M. Farine, Nucl. Phys. A **454**, 374 (1986).

[68] M. Kortelainen, T. Lesinski, J. Moré, W. Nazarewicz, J. Sarich, N. Schunck, M. V. Stoitsov, and S. Wild, Phys. Rev. C **82**, 024313 (2010).

[69] M. Kortelainen, J. McDonnell, W. Nazarewicz, P.-G. Reinhard, J. Sarich, N. Schunck, M. V. Stoitsov, and S. M. Wild, Phys. Rev. C **85**, 024304 (2012).

[70] E. Chabanat, P. Bonche, P. Haensel, J. Meyer, and R. Schaeffer, Nucl. Phys. A **635**, 231 (1998); **643**, 441 (1998).

[71] X. Roca-Maza, M. Brenna, B. K. Agrawal, P. F. Bortignon, G. Colò, L.-G. Cao, N. Paar, and D. Vretenar, Phys. Rev. C **87**, 034301 (2013).

[72] J. M. Pearson, S. Goriely, and N. Chamel, Phys. Rev. C **83**, 065810 (2011).

[73] J. M. Pearson, N. Chamel, S. Goriely, and C. Ducoin, Phys. Rev. C **85**, 065803 (2012).

[74] J. Erler, C. J. Horowitz, W. Nazarewicz, M. Rafalski, and P.-G. Reinhard, Phys. Rev. C **87**, 044320 (2013).